Published in final edited form as:
Nat Neurosci. ; 15(7): 988–997. doi:10.1038/nn.3137.

Release probability of hippocampal glutamatergic terminals scales with the size of the active zone

Noemi Holderith[1], **Andrea Lorincz**[1], **Gergely Katona**[2], **Balázs Rózsa**[2], **Akos Kulik**[3,4], **Masahiko Watanabe**[5], and **Zoltan Nusser**[1]

[1]Laboratory of Cellular Neurophysiology, Institute of Experimental Medicine, Hungarian Academy of Sciences, Budapest, HUNGARY

[2]Two-Photon Imaging Center, Institute of Experimental Medicine, Hungarian Academy of Sciences, Budapest, HUNGARY

[3]Institute of Anatomy and Cell Biology, Department of Neuroanatomy, Department of Physiology II, University of Freiburg, Freiburg, Germany

[4]BIOSS Centre for Biological Studies, University of Freiburg, Freiburg, Germany

[5]Department of Anatomy, Hokkaido University School of Medicine, Sapporo, Japan

Abstract

Cortical synapses display remarkable structural, molecular and functional heterogeneity. Our knowledge regarding the relationship between the ultrastructural and functional parameters is still fragmented. Here we asked how the release probability and presynaptic [Ca^{2+}] transients relate to the ultrastructure of rat hippocampal glutamatergic axon terminals. Two-photon Ca^{2+} imaging-derived optical quantal analysis and correlated electron microscopic reconstructions revealed a tight correlation between the release probability and the active zone area. The peak amplitude of [Ca^{2+}] transients in single boutons also positively correlated with the active zone area. Freeze-fracture immunogold labeling revealed that the voltage-gated Ca^{2+} channel subunit Cav2.1 and the presynaptic protein Rim1/2 are confined to the active zone and their numbers scale linearly with the active zone area. Gold particles for Cav2.1 showed a nonrandom distribution within the active zones. Our results demonstrate that the number of several active zone proteins, including presynaptic Ca^{2+} channels, docked vesicles and the release probability scales linearly with the active zone area.

Introduction

Synapses display enormous diversity in their structure and function. Even in a homogeneous population of connections between two well-defined cell types, large variability is found in the shape and size of pre- and postsynaptic elements[1,2]. Similar to the structural diversity, many functional parameters such as the probability of the transmitter release, the size of the readily releasable pool of vesicles, short- and long-term plasticity of the synapses and the

Correspondence to: Zoltan Nusser, Laboratory of Cellular Neurophysiology, Institute of Experimental Medicine, Hungarian Academy of Sciences, Szigony Street 43, 1083 Budapest, HUNGARY Tel.: 36 1 210 9983, Fax: 36 1 210 9984, nusser@koki.hu.

Author's contributions: NH performed all *in vitro* Ca^{2+} measurements and *post hoc* light- and electron microscopic analysis of the imaged structures. AL performed SDS-FRL for SNAP-25, Cav2.1 and Rim1/2, quantitatively analyzed the reactions, and performed the simulations. GK developed the image acquisition and analysis software. BR designed and built the two-photon microscope. AK performed SDS-FRL reactions for Cav2.1 in Cav2.1$^{+/-}$ and Cav2.1$^{-/-}$ mice. MW developed the guinea pig anti-Cav2.1 antibody. NH and ZN designed the experiments and wrote the manuscript.

Competing financial interest: BR and GK are the owners of Femtonics Ltd.

Europe PMC Funders Author Manuscripts

size of the postsynaptic responses display large heterogeneity[3]. Although tremendous efforts have been invested in the past decades, the contribution of differences in the synaptic ultrastructure or the molecular composition of synapses to generating functional diversity is still debated. An example of an apparent relationship between synapse ultrastructure and function comes from studies examining the numbers and densities of postsynaptic AMPA and NMDA-type glutamate receptors. Both receptor types are concentrated in the postsynaptic density (PSD), and their numbers scale with the PSD area[4-6]. As a consequence, larger postsynaptic responses are generated in larger spines[7,8] with larger PSDs[9]. Clearly, the actual size of the PSD has very little direct effect on the amplitude of the postsynaptic response, but because the PSD area tightly correlates with the number of postsynaptic glutamate receptors, it can be used to predict the size of the postsynaptic response. Can a similar ultrastructural feature that is indicative of function be found on the presynaptic side? Most presynaptic axons that were initially examined to address this question are large, contain a large number of active zones and are specialized for rapid, reliable excitation of their postsynaptic partners (e.g. neuromuscular junction, squid giant axon, calyx of Held). Many of the classical papers indicated a correlation between the structure and function of these large axons/axon terminals[10-13]. However, most axon terminals in the CNS are small, often bear a single active zone and cannot efficiently drive their postsynaptic target cells. This is particularly true for cortical glutamatergic terminals, which are in the order of 1 μm in diameter; most of them have a single active zone; and their release probabilities range from 0 to 0.9. The long-standing question is to what extent can the morphological parameters of cortical glutamatergic terminals predict their functional properties? Studies of cultured hippocampal neurons suggested that the release probability correlates with the number of readily releasable vesicles, which corresponds to vesicles docked at the presynaptic active zone[14,15]. In the same synapse population, the number of docked vesicles has been found to be proportional to the active zone area and to the volume of the terminal[1,2], implying that the larger the presynaptic terminal, the higher its release probability is. The general applicability of such a clear correlation was challenged by data showing that glutamatergic terminals of cortical and hippocampal pyramidal cells, which are presynaptic to distinct types of GABAergic interneurons, possess widely different release probabilities and short-term plasticity patterns[16-20], but have very similar sizes. Similarly, axon terminals of the cerebellar cortex with similar active zone sizes and number of docked vesicles display dramatically different release probabilities[21], indicating that the molecular composition of the presynaptic terminal must play a key role in determining the functional properties. To overcome potentially diversifying factors we decided to examine a homogeneous population of axon terminals of CA3 pyramidal cells synapsing on other CA3 pyramidal cells in acute hippocampal slices. We addressed the relationship between the ultrastructure, molecular composition and function of these terminals by combining *in vitro* patch-clamp electrophysiology, two-photon fluorescent Ca^{2+} imaging with multiple line scanning, *post hoc* electron microscopic 3D reconstruction of the imaged pre- and postsynaptic structures and quantitative, SDS-digested freeze-fracture replica immunogold localization (SDS-FRL) of presynaptic proteins.

Results

Morphological diversity of hippocampal CA3 pyramidal cell axon terminals

Schaffer collateral synapses made by CA3 pyramidal cell axons onto CA1 pyramidal cell dendrites differ greatly from one another with respect to their morphological and functional parameters[1,2]. However, the long distance between the cell bodies of CA3 pyramidal cells and their boutons in the CA1 area imposes a long diffusion time of Ca^{2+} sensitive fluorescent dyes to the terminals when introduced somatically. We therefore chose the local axon collaterals of pyramidal cells in the CA3 stratum oriens within 150-300 μm from the

somata. These axon terminals establish synapses both on the basal dendritic spines of other CA3 pyramidal cells and on local GABAergic interneurons. In the present work, we focused exclusively on pyramidal cell – pyramidal cell synapses. Because quantitative information regarding the morphological properties of these synapses was not available, we first performed electron microscopic 3D reconstructions from serial ultrathin sections of a 16 day-old rat. Figure 1 illustrates local axon terminals and their postsynaptic pyramidal cell spines, displaying substantial variability in the volume of the boutons (0.18 ± 0.14 μm^3, n = 68, Fig. 1h), in the area of the active zones (0.04 ± 0.03 μm^2, n = 83, Fig. 1i) and in the volume of the postsynaptic spines (0.04 ± 0.04 μm^3, n = 83, Fig. 1j). The majority of the boutons formed synapses with only a single postsynaptic partner, whereas approximately one fifth of the boutons had more than one postsynaptic target (13.2% had two, 4.4% had three, 1.5% had four). Individual active zone areas showed only a weak positive correlation with the volume of the bouton (Fig. 1k) and the volume of the presynaptic terminal poorly predicted the volume of the postsynaptic spine (Fig. 1l). However, the total active zone area (calculated by summing up all active zones per bouton) displayed a tighter correlation with the volume of the boutons (R = 0.68). Virtually all CA3 pyramidal cell spines had a single presynaptic partner, and consequently had a single PSD, the size of which reliably predicted the volume of the spine (Fig. 1m). Axon terminals contain a large number of small synaptic vesicles. Few of these vesicles are within few nanometers from the presynaptic active zone membrane (docked vesicles, Fig. 2a, b) and may correspond to the functionally defined readily releasable pool. Most vesicles are tens and hundreds of nanometer away from the active zone and might comprise the reserve pool. For assessing the number of docked vesicles possibly the best method is electron microscopic tomography. However, a reliable estimate can also be obtained with electron microscopic 3D reconstruction from very thin sections. We chose the second method and reconstructed 15 synapses (n = 1 animal) from 20 nm thin sections (Fig. 2c) and found that the number of docked vesicles positively correlates with the active zone area (Fig. 2d). The ultrastructural parameters described above are very similar to those published previously for Schaffer collateral synapses in the CA1 area[1,2] and also predict a large heterogeneity in their functional properties.

Large variability in release probability and short-term plasticity of axon terminals

To measure the release probability and short-term plasticity of CA3 pyramidal cell local axon collaterals, we performed two-photon imaging of $[Ca^{2+}]$ transients in individual dendritic spines in response to paired extracellular stimulation. By holding pyramidal cells at −30 mV, Ca^{2+} fluxing through NMDA receptors following the presynaptic release of glutamate could be efficiently detected in single spines and the successful events could be reliably distinguished from the failures (Fig. 3a-c; Supplementary Fig. 1). Repeating the stimulations 50 – 120 times allowed the determination of the release probability[22]. This release probability denotes to the probability that neurotransmitter release occurs from a given active zone and it is different from vesicle release probability. To increase the chance of finding spines postsynaptic to activated boutons, we placed a unipolar stimulating electrode a few tens of microns away from the monitored basal dendrite and simultaneously imaged 6 – 12 spines within a dendritic segment using a line scanning mode (Fig. 3d, e). Figure 3d-h shows a typical example of simultaneously monitoring 9 spines and 2 dendritic shaft segments. Rapidly rising, transient increases in $[Ca^{2+}]$ were visible (detected with 100 μM Fluo5F, a pseudo-colored single trial response is shown in Fig. 3e) in 2 out of 9 spines, whereas delayed, slow rising, small amplitude transients could be detected in some of the neighboring spines and dendritic shafts. Boutons with different release probabilities established synaptic contacts with spines close to each other on a short dendritic segment (Fig. 3g-h, e.g. spine #3: release probability = 0.02, spine #9: release probability = 0.11). Examining 43 activated spines (in 14 animals) revealed a great variability in the release probability for the 1st (P_R^{1st}) and 2nd (P_R^{2nd}) stimuli among axon terminals (P_R^{1st}: range: 0

– 0.53, mean ± SD = 0.14 ± 0.14; P_R^{2nd} range: 0.03 – 0.48, mean ± SD = 0.19 ± 0.12, n = 43 spines; Fig 3i). We also determined the paired-pulse plasticity (at 100 ms inter-stimulus interval) of release by dividing the P_R^{2nd} with P_R^{1st} for each bouton. Our results demonstrate a wide range of paired-pulse ratios (PPR, 0.43 – 10) with an average of ~2-fold facilitation (mean ± SD = 2.2 ± 2.0, n = 40 synapses; three synapses had a P_R^{1st} of 0). There was an inverse correlation between the P_R^{1st} and the PPR for these axon terminals; synapses with a $P_R^{1st} < 0.1$ always displayed paired-pulse facilitation (mean PPR = 3.15), whereas those with a $P_R^{1st} > 0.4$ always showed paired-pulse depression (mean PPR = 0.71). Our results revealed a large heterogeneity in the functional properties of CA3 pyramidal cell local axon collaterals, similar to that of Schaffer collaterals in acute slices and cultures.

Having established a large diversity in both the ultrastructural and functional properties of CA3 pyramidal cell axon terminals, next we examined the correlations among the measured structural and functional parameters. In addition to the Ca^{2+}-sensitive (Fluo5F, 100 μM) and insensitive (20 μM Alexa594) fluorescent dyes, we also included biocytin in the intracellular solution, allowing *post hoc* light microscopic and subsequent electron microscopic visualization of the imaged dendritic segments. Seven spines and their parent dendrite (Fig. 4a) were simultaneously scanned, out of which two spines (s2 and s4) had fast rising $[Ca^{2+}]$ transients in response to extracellular stimulations. Bouton #4 had a low P_R^{1st} (0.08; Fig. 4b), whereas bouton #2 had relatively high P_R^{1st} (0.33; Fig. 4c). The whole dendritic segment was electron microscopic 3D reconstructed from serial ultrathin sections (Fig. 4d, e) and all seven imaged spines were identified on the reconstructed profile (Fig. 4f). Following the identification of the activated spines (s2 and s4), we also reconstructed the unlabeled axon terminals that made synaptic contacts onto these spines (blue profiles in Fig. 4d-f). Both spines had only a single presynaptic partner. Our *post hoc* 3D reconstructions revealed differences in both the volume of the boutons and the area of the active zones. Examining the relationships between the P_R^{1st} and the volume of the boutons (Fig. 4g) and between the P_R^{1st} and the area of the active zone (Fig. 4h) for all reconstructed synaptic partners revealed significant ($p < 0.01$) positive correlations (n = 14 synapses in 6 animals).

Variability in $[Ca^{2+}]$ in CA3 pyramidal cell axon terminals

The probability of transmitter release depends on the spatio-temporal profile of free $[Ca^{2+}]$ around the docked vesicles and the binding rate of Ca^{2+} to the sensor. Despite the wealth of information regarding the relationship between $[Ca^{2+}]$ and release obtained at the neuromuscular synapse, the squid giant axon, the calyx of Held and hippocampal basket cell terminals[23-29], almost nothing is known about these parameters at cortical glutamatergic terminals. Koester and Sakmann[30] measured volume-averaged $[Ca^{2+}]$ in cortical layer 2/3 pyramidal cell axon terminals and found a greater than 10-fold variability in the peak $[Ca^{2+}]$. Because direct measurements of the release probability and AP-evoked $[Ca^{2+}]$ in individual small cortical glutamatergic terminals is not possible with currently available techniques in acute slices, we chose a strategy to determine these functional parameters in separate sets of experiments and relate both of them to the same set of ultrastructural parameters. We measured single AP-evoked $[Ca^{2+}]$ transients in the boutons of CA3 pyramidal cell local axon collaterals (See Methods and Supplementary Figs. 2 and 3) in the stratum oriens followed by *post hoc* electron microscopic 3D reconstruction of the imaged boutons. The peak amplitude of the $[Ca^{2+}]$ transients displayed large (8-fold) variability among the boutons (mean ± SD = 0.16 ± 0.07 G/G_{MAX}; coefficient of variation = 0.45, n = 84 boutons in 4 animals; Fig. 5a-e). Following fixation, we visualized the biocytin and identified the individual imaged boutons at the light microscopic level (Fig. 5f) and also on serial electron microscopic sections. For 27 boutons (from 4 animals), we could also faithfully identify pyramidal cell spines as their single postsynaptic targets (Fig. 5h, i) and

perform full 3D reconstructions of both the pre- and postsynaptic elements. Two boutons with very similar volumes (marked by blue and green dots, 0.22 and 0.24 μm^3, respectively, Figure 5g-i) displayed an ~2.5-fold difference in their peak [Ca^{2+}] transients. In agreement with these examples, we could not find a significant correlation between the bouton volume and the amplitude of the [Ca^{2+}] transients (Fig. 5j). However, when we examined the correlation between the amplitude of the [Ca^{2+}] transients and the active zone area (Fig. 5k) and the total amount of fluxed Ca^{2+} per AP and the active zone area (Fig. 5l), significant ($p < 0.01$) positive correlations were found. The two boutons illustrated in figure 5h and i had an active zone area ratio of 2.4, a peak [Ca^{2+}] ratio of 2.5 and a total fluxed Ca^{2+} ratio of 2.3.

Contribution of Ca^{2+} channel subtypes to [Ca^{2+}] in boutons

Excitatory postsynaptic responses of hippocampal glutamatergic synapses are mediated by a concerted action of several types of voltage-gated Ca^{2+} channels (Cav), each with distinct pharmacological profiles[31-33]. Here we examined the direct contribution of these channel subtypes to [Ca^{2+}] transients measured in individual boutons of CA3 pyramidal cells (Supplementary Fig. 4). The Cav2.1 (P/Q-type) subunit-specific blocker ω-ATX-IVA (1 μM) and the Cav2.2 (N-type) subunit-specific blocker ω-CTX-GVIA (1 μM) reduced the peak amplitude of the [Ca^{2+}] transients by 28.8 ± 1.1 % (Supplementary Fig. 4a, n = 67 boutons in 4 cells from 4 animals, $p<0.0001$) and 35.7 ± 12 % (Supplementary Fig. 4b, n = 71 boutons in 4 cells from 4 animals, $p<0.0001$), respectively. Application of SNX482 (500 nM), a Cav2.3 (R-type) subunit-specific blocker, resulted in a 14.7 ± 2.3 % reduction in the peak amplitude (Supplementary Fig. 4c, n = 40 boutons in 3 cells from 3 animals, $p<0.01$). These results on the pharmacological profile of the presynaptic [Ca^{2+}] transients are in agreement with previous data showing a major role of the Cav2.1, Cav2.2 and Cav2.3 subunits in mediating postsynaptic responses at hippocampal glutamatergic terminals[32] and that of bulk Ca^{2+} imaging of Schaffer collateral terminals[31]. Following the blockade of Cav2.2 and Cav2.3 subunits, when the majority of the Ca^{2+} influx is mediated by the Cav2.1 subunit, the amplitude of the [Ca^{2+}] transients was reduced by 50.4 ± 3.9 % (n = 39 boutons in 2 cells from 2 animals), but the bouton-to-bouton variability of the responses remained very similar (coefficient of variation = 0.51), demonstrating that the large variability in peak [Ca^{2+}] is also evident under conditions when mainly Cav2.1 channels mediate the Ca^{2+} influx.

The Cav2.1 subunit is confined to the presynaptic active zone

Assuming that Cav channels are confined to the active zone membrane of the bouton, our Ca^{2+} imaging experiments, revealing that the total amount of fluxed Ca^{2+} following an AP is proportional to the active zone area, predict that the number of Cav channels scales linearly with the active zone area. However, direct experimental data for cortical excitatory axon terminals was not available regarding this important assumption. Therefore, we carried out high-resolution SDS-FRL of the Cav2.1 subunits in the stratum oriens of adult and 16 days-old rats (Fig. 6). In this technique, following rapid freezing and fracturing of brain tissue, carbon-platinum-carbon replicas are created from the fractured tissue surfaces. Fractured membranes containing transmembrane proteins attached to the replica will be retained following digestion with SDS, and can be visualized with electron microscopic immunogold techniques (see Methods, reviewed by ref. 34). In adult rats, immunogold particles labeling the Cav2.1 subunit on protoplasmic (P-face) plasma membranes were highly enriched in presynaptic active zones compared to extrasynaptic bouton surfaces (Fig. 6a). A similar enrichment of the Cav2.1 subunit in the active zones was found in rats age-matched (P16) to those used in our imaging experiments (Fig. 6b). The active zones were recognized from the clusters of intramembrane particles (IMP)[35]. To provide molecular evidence that the site of Ca^{2+} channel clustering is indeed the active zone, we performed

double immunolabeling for the Cav2.1 subunit and presynaptic active zone proteins Rim1/2 (Fig. 6c) and found that both were confined to the same part of the presynaptic plasma membrane; to the active zone. Furthermore, we carried out double immunogold labeling for Cav2.1 and AMPA type glutamate receptors. Small gold particles labeling the Cav channels were accumulated in presynaptic specializations facing AMPA receptor immunopositive PSDs in synapses in which both the presynaptic P-face and the corresponding postsynaptic extracellular (E-face) membranes were exposed (Fig. 6d). Finally, we performed two series of experiments to validate the specificity of Cav2.1 immunolabeling in our replicas. First, we carried out SDS-FRL with another anti-Cav2.1 subunit antibody (rabbit) that was raised against a different epitope of the protein and obtained a qualitatively very similar result to that obtained with our guinea pig anti-Cav2.1 antibody. In double labeling reactions, the two antibodies labeled exactly the same subcellular compartment of CA3 pyramidal cell axon terminals (Fig. 6e). In a second set of experiments, we performed SDS-FRL on hippocampal tissue of Cav2.1$^{+/-}$ and Cav2.1$^{-/-}$ mice. The labeling pattern on Cav2.1$^{+/-}$ tissue was similar to that observed in Wistar rats (Fig. 6f); an extensive colocalization of the Cav2.1 was observed with Rim1/2. In contrast, Rim1/2 positive active zones in Cav2.1$^{-/-}$ mice were always immunonegative for the Cav2.1 subunit (Fig. 6g). Quantitative analysis revealed that in Cav2.1$^{+/-}$ tissue a total of 211 gold particles labeling Cav2.1 were detected in 39 active zones, whereas in Cav2.1$^{-/-}$ mice, zero particle was found in 24 Rim1/2-positive active zones. In agreement with our electron microscopic immunogold data, when slowly rising, small amplitude [Ca^{2+}] transients were recorded in five presynaptic boutons, *post hoc* electron microscopic analysis revealed the lack of postsynaptic partners and active zones (Supplementary Fig. 5). The slow rise times and small amplitudes are inconsistent with the direct entry of Ca^{2+}, but consistent with the diffusion of Ca^{2+} or Ca^{2+}-bound Fluo5F from a neighboring bouton, which was just few microns away.

Rim1/2 and Cav2.1 have uniform densities in presynaptic active zones

Optical quantal analysis followed by *post hoc* electron microscopic 3D reconstructions demonstrated that the release probability scales quasi-linearly with the size of the presynaptic active zone. A prediction of this result is that large presynaptic active zones consist of multiple neurotransmitter release sites. If a functional release site is created by a defined number of molecules associated with the active zone, then the prediction of our results is that the number of presynaptic active zone proteins should scale linearly with the active zone area. We tested this prediction by performing quantitative electron microscopic immunogold localization of active zone proteins. First we tested the distribution of SNAP-25, a SNARE protein, and found that immunogold particles were present within and outside the active zones (Fig. 7a, b). Quantitative analysis revealed that the density of SNAP-25 in the active zone was very similar to that found on the non-synaptic part of the bouton (Fig. 7d), consistent with the results of Hagiwara et al.[35]. We also confirmed the results of Hagiwara et al.[35] that syntaxin-1B is also present rather uniformly in the synaptic and non-synaptic plasma membranes. Synaptobrevin was mainly found on synaptic vesicles with a low intensity labeling on the plasma membranes. With such proteins, the above-mentioned prediction could not be tested. We therefore searched for presynaptic proteins with an exclusive active zone location. The most obvious one was the Cav2.1 subunit. A smaller number of gold particles was found in smaller active zones (Fig. 7e, f). There was a steep, significant positive linear correlation ($p < 0.01$ in both animals) between the number of gold particles and the active zone area (Fig. 7g). Quantification of the immunolabeling revealed a high density of gold particles in the active zones, but the extrasynaptic densities did not significantly differ ($p = 0.73$ and 0.06 in two animals) from the background (Fig. 7h). Finally, Rim1/2 was also restricted to the active zone (Fig. 7i-l). Similar to our results with the Cav2.1 subunit, the number of gold particles labeling Rim1/2 also displayed a tight, significant positive correlation ($p < 0.01$ in both animals) with the active zone area (Fig. 7k).

We also noticed that gold particles labeling Cav2.1 were not distributed uniformly within the active zones, but seemingly formed small clusters (e.g. Figs. 6a, 7e, 8a). To quantitatively analyze the distribution of Cav2.1 immunolabeling within the active zone (Fig. 8), we measured all inter-gold distances within individual active zones and asked the question whether the inter-gold distance distribution was significantly different from random distributions (Fig. 8a_3, b_3, c_4). For this, we generated 50 random distributions for each synapse having exactly the same number of 'gold' particles as determined experimentally in the same synapse (Fig. 8a_4, b_4, c_3) and calculated the distributions of the simulated inter-'gold' distances. For large active zones (>0.1 μm^2) where a large number of gold particles were detected, in >50% of the active zones the inter-gold distance distributions were significantly ($p < 0.05$, for all 50 random distributions) different from random distributions. This proportion was 26% for all examined presynaptic active zones (n = 34; Fig. 8d). For many small active zones with a small number of gold particles, the inter-gold distance distributions could be either significantly or non-significantly different from random distributions (Fig. 8b_3, c_4).

Discussion

In the present manuscript, we describe a large heterogeneity in the morphological, molecular and functional properties of local axon collaterals of CA3 pyramidal cells. We reveal that the release probability of individual terminals as well as the total amount of fluxed Ca^{2+} following an AP scales linearly with the active zone area. We also found that the Cav2.1 subunits are concentrated in the presynaptic active zone, and their numbers together with that of Rim1/2 are proportional to the active zone area. These results, taken together are consistent with a modular model of the active zone[36], where the number of functional release sites scales with the active zone area and, as a consequence, enables release at multiple sites at large pyramidal cell – pyramidal cell synapses.

Our results obtained with functional and morphological examinations of CA3 pyramidal cell – pyramidal cell glutamatergic synapses revealed large structural and functional heterogeneities within this apparently homogeneous synapse population. It has been known that both the pre- and postsynaptic properties of central synapses depend on the cellular identity of the synapsing partners. For example, the release probability and short-term plasticity of release from hippocampal and cortical pyramidal cell axon terminals depends on the target cell type; pyramidal cells evoke facilitating EPSPs on hippocampal OLM and neocortical bitufted interneurons, whereas the same presynaptic pyramidal cells innervate parvalbumin positive basket cells with depressing EPSPs[16-20]. These target cell type-specific differences have been shown to be reflected in the amplitude of $[Ca^{2+}]$ transients in the presynaptic boutons[18]. The identity of the presynaptic cell type is also instrumental in setting the functional and structural parameters of the synapses. For example, parallel and climbing fiber synapses on cerebellar Purkinje cells have widely different initial release probabilities and short-term plasticity[21]. Similarly, the release properties of CCK and parvalbumin expressing hippocampal basket cells are also different[37]. Thus, if one examines a synapse population in which the pre- and postsynaptic cellular elements are heterogeneous (e.g. synapses in the neocortex), it is not surprising to see large structural and functional diversity. Keeping this in mind, we restricted our analysis to CA3 pyramidal cell local axon terminals that formed synapses only onto other CA3 pyramidal cell spines, and still observed an extensive functional and structural heterogeneity. This large diversity of synapses seems to be a unique feature of pyramidal cells, because when other synapse populations are examined, which have homogeneous pre- and postsynaptic cellular elements (e.g. parvalbumin positive basket cells onto dentate gyrus granule cells, globular bushy cells of the ventral cochlear nucleus onto principal cells of the medial nucleus of the trapezoid body, i.e: calyx of Held, etc.), a much smaller heterogeneity is found in the initial release

probability, short-term plasticity and size of the active zones. This is probably a reflection of the more plastic properties of pyramidal cell – pyramidal cell connections and their widely different functional states at any given time in the life of an animal. However, it cannot be excluded that a similar degree of heterogeneity will be found in synapses that show much less plasticity. Irrespective of this, here we present quantitative data regarding the distribution of many morphological and functional parameters of CA3 pyramidal cell – pyramidal cell synapses, providing essential information for constructing realistic neuronal network models and forming the foundation for comparisons of different physiological and pathological network states.

Revealing the coupling between the presynaptic Ca^{2+} channels and the Ca^{2+} sensor of the release machinery is fundamental to our understanding of synaptic communication between nerve cells. The complexity of determining the exact relationship of the Ca^{2+} – release coupling has been widely appreciated[26,38]. It requires quantitative knowledge about the number, density and distribution of presynaptic Ca^{2+} channels at the active zone; the location and the kinetic properties of the Ca^{2+} sensors; the concentration and binding kinetics of fixed and mobile Ca^{2+} buffers and their diffusion coefficients. Recent experiments, using exogenously applied fast and slow Ca^{2+} buffers revealed two fundamentally different modes of Ca^{2+} – release coupling. At hippocampal parvalbumin positive basket cell synapses[39], retinal ribbon synapses[40], cerebellar basket cell synapses[41] and in adult calyx of Held synapses[42], the slow Ca^{2+} buffer EGTA at low mM concentrations cannot interfere with neurotransmitter release, indicating that the distance between the Ca^{2+} entry site and the sensor is short, probably in the range of tens of nanometers (nanodomain coupling). In addition, in these synapses, the number of Ca^{2+} channels mediating the release of a single vesicle is low (between 1 and 5; ref. 38). However, at young calyx of Held[43], cortical CCK-positive basket cell[37] and cortical pyramidal cell synapses[19,44], EGTA at concentrations of a few mM strongly reduces postsynaptic responses, indicating a larger distance (from fifty to few hundred nm) between the Ca^{2+} channels and the sensors (microdomain coupling). This regime also predicts a much larger number of Ca^{2+} channels contributing to the Ca^{2+} concentration that drive synchronous release. Although these experiments provide functional data regarding the number of release-associated Ca^{2+} channels and the distance between the Ca^{2+} channels and the sensors, they could not reveal where exactly the Ca^{2+} channels are located on the surface of a bouton, or what their densities are within and outside the active zone.

Long-standing questions in this field are whether Ca^{2+} channels are confined to the presynaptic active zone and whether they have a random, or non-random (e.g. uniform, clustered) distribution within the active zone. Many investigators attempted to address this issue using many different techniques and preparations in the past three decades. Llinas et al.,[45] recorded Ca^{2+} microdomains in the squid giant axon in localized spots assumed to be active zones. Similar highly localized Ca^{2+} microdomains were detected in cultured neuromuscular junctions by DiGregorio et al.[46] and by Frank et al.[47] in inner hair cells. However, none of these papers provided direct evidence that these domains corresponded to active zones. When similar fluorescent [Ca^{2+}] measurements were performed in small CNS boutons, no spatial inhomogeneities could be detected due to the small size of the boutons, the rapid equilibration of Ca^{2+} within the terminal and the relatively slow binding rate of Ca^{2+} to the employed Ca^{2+} sensitive fluorescent reporters[18,25,30]. In summary, current Ca^{2+} imaging experiments could not provide information regarding the distribution of Ca^{2+} channels within small glutamatergic or GABAergic boutons.

A more appropriate method to reveal the precise distribution of Ca^{2+} channels within axon terminals is immunolocalization or fluorescent tagging and examining the reactions with light- or electron microscopy. In Drosophila neuromuscular junctions, RIM-binding protein

(DRBP) plays a key role in the molecular integrity of the active zone and in the active zone localization of the Ca^{2+} channels[48]. Super-resolution light microscopic experiments provided compelling evidence for the active zone location of Ca^{2+} channels, but how their number or density relate to the size of the active zone remained unknown.

In the present manuscript, we applied high-resolution electron microscopic immunogold localization of the Cav2.1 subunit and found their exclusive active zone location in CA3 pyramidal cell local axon terminals. Recent immunolocalization experiments using a pre-embedding electron microscopic immunogold technique demonstrated the enrichment of Cav2.1 in the active zones of cerebellar parallel fiber[49] and hippocampal fast spiking basket cells terminals[39]. Across the active zones of CA3 pyramidal cells, the density of Cav2.1 channels was uniform, similar to that of the active zone-related proteins Rim1/2. The uniform Rim1/2 and Cav2.1 densities predict that larger active zones will have proportionally more molecular resources for supporting release. Notably, in large active zones where many gold particles were found, they did not show a random distribution within the active zone. This nonrandom Ca^{2+} channel distribution might indicate that the sites of vesicle docking and release cannot occur anywhere within the active zone, but only in molecularly-defined spaces. As described above, the coupling between Ca^{2+} channels and the sensor is not very tight in cortical pyramidal cell axon terminals[44]. Although the exact distance between them has not been identified with detailed modeling, a minimum distance of ~100 nm is estimated[38]. Building on this assumption, we calculated that every Ca^{2+} channel within an active zone area of 0.01 μm^2 will contribute to the release of a vesicle. In our immunogold reactions, we detected ~400 gold particles in each μm^2 of active zone membrane, demonstrating a minimum of 4 Cav2.1 channels within an active zone area of 0.01 μm^2. This calculation assumes a 100% labeling efficiency, which is possible to achieve with SDS-FRL[50]. However, we have no information regarding our labeling efficiency, and therefore only a lower limit on the number of Ca^{2+} channels can be provided. Our pharmacological experiments demonstrated that only ~30% of the Ca^{2+} enters the terminals through Cav2.1 channels. If the Cav2.2 and Cav2.3 subunit-containing channels are also confined to the active zone, and if they have a similar single channels conductance and open probability, we could estimate a minimum of 14 presynaptic Ca^{2+} channels contributing to the Ca^{2+} microdomain seen by the Ca^{2+} sensor of a vesicle in CA3 pyramidal cell axon terminals.

Methods

Slice preparation and electrophysiological recordings

Acute 300 μm thick horizontal ventral hippocampal slices were cut from male Wistar rats (14–17 days old). Animals were killed by decapitation, in accordance with the Hungarian Act of Animal Care and Experimentation (1998, XXVIII, section 243 / 1998), and with the ethical guidelines of the Institute of Experimental Medicine Protection of Research Subjects Committee. The brain was quickly removed and placed into an ice-cold cutting solution containing (in mM): sucrose, 205.2; KCl, 2.5; $NaHCO_3$, 26; $CaCl_2$, 0.5; $MgCl_2$, 5; NaH_2PO_4, 1.25; glucose, 10; saturated with 95 % O_2 and 5 % CO_2. Hippocampal slices were prepared using a Leica vibratome (Leica VT1200S; Leica Microsystems, Vienna, Austria), incubated in an interface-type holding chamber[51] in ACSF containing in mM: NaCl, 126; KCl, 2.5; $NaHCO_3$, 26; $CaCl_2$, 2; $MgCl_2$, 2; NaH_2PO_4, 1.25; glucose, 10 saturated with 95 % O_2 and 5 % CO_2 (pH = 7.2 – 7.4) at 36°C that was then gradually cooled down to room temperature (~1 h). Recordings were carried out in the same ACSF, slices were kept up to 6 hours in the holding and recording chambers. Extracellularly evoked spine Ca^{2+} responses were measured in ACSF supplemented with 10 μM D-serine, 5 μM NBQX and 20 μM SR59931.

Cells were visualized using a Femto2D microscope equipped with oblique illumination and a water immersion lens (25X, 1.05 NA, Olympus, Japan). Current-clamp whole-cell recordings from the soma of hippocampal CA3 pyramidal cells were performed using a MultiClamp 700A amplifier (Molecular Devices), traces were filtered at 3 kHz and digitized on-line at 20 kHz. Series resistance was < 20 MΩ. Patch pipettes were pulled (Zeitz Universal Puller; Zeitz-Instrumente Vertriebs, Munich, Germany) from thick-walled borosilicate glass capillaries with an inner filament (1.5 mm outer diameter, 0.86 mm inner diameter; Sutter Instruments, Novato, CA). Pipette resistance was 3–6 MΩ when filled with the intracellular solution containing in mM: K-gluconate, 110; KCl, 5; creatine phosphate, 10; HEPES, 10; ATP, 2; GTP, 0.4; biocytin, 5 and 100 – 300 μM Fluo5F (Molecular Probes, K_D ~ 1.1 μM) and 20 μM Alexa594 (Molecular Probes; pH = 7.3; 290–300 mOsm). For postsynaptic spine [Ca^{2+}] measurements, 5 mM QX-314 [N-(2,6-dimethylphenylcarbamoylmethyl)-triethylammonium bromide] was added into the intracellular solution.

Pyramidal cells were held at −70 mV (with 0 to −100 pA current injection) and single action potentials (APs) at 0.016 Hz were evoked with 2–3 ms-long depolarizing current pulses (1–1.2 nA). Peak amplitude and full width at half maximal amplitude of the APs were monitored throughout the recordings and cells were rejected if any of these parameters changed more than 10%. ω-Conotoxin GVIA (ω-CTX GVIA 1 μM, Tocris; Product #1085), ω-agatoxin IVA (ω-ATX, 1 μM, Alomone Labs #RTA-500 and Tocris; #2799) and SNX 482 (500 nM, Tocris; #2945) were applied using a recirculation system with a peristaltic pump. The total volume was ~8 ml, and the solution was equilibrated with 95% O_2 and 5% CO_2. Bovine serum albumin was added at a concentration of 1 mg/ml. For extracellularly evoked responses a unipolar stimulating electrode was placed in the str. oriens at ~40 μm distance from a selected basal dendritic region of a CA3 pyramidal cell that was recorded in whole-cell mode for > 40 min and depolarized to −30 mV to relieve the Mg^{2+} block of NMDA receptors. Pairs of stimuli (30–100 μA) at 10 Hz were applied and were repeated in every minute. All recordings were carried out at 24°C. All drugs were purchased from Sigma unless indicated otherwise.

Two photon imaging

Experiments were performed with a Femto2D (Femtonics Ltd., Budapest, Hungary) laser scanning microscope[52] with a MaiTai femtosecond pulsing laser (MaiTai, SpectraPhysics, Mountain View, CA) tuned to 810 nm. Both reflected and transmitted (through an oil-immersion condenser, Olympus, NA = 1.4) fluorescent light were collected. Electrophysiological data and image acquisition was controlled by custom made software written in MATLAB (MES, Femtonics Ltd.).

Cells were filled with two fluorescent dyes: a Ca^{2+}-insensitive fluorophore (Alexa594, 20 μM), and a Ca^{2+}-sensitive fluorophore (Fluo5F, 100–300 μM). Red fluorescence was used to identify spines and boutons. Changes in fluorescence were quantified during the recording as:

$$\Delta G/R\,(t) = \left(F_{green(t)} - F_{rest,green}\right) / \left(F_{green} - I_{dark,red}\right).$$

$F_{green(t)}$ is the green fluorescence signal as a function of time, $F_{rest,green}$ is the green fluorescence before stimulation, and $I_{dark,red}$ is the dark current in the red channel. G/R was separately measured in saturating [Ca^{2+}] (G_{MAX}/R) for each dye combination and batch of intracellular solution by imaging a sealed pipette filled with a mixture of equal volumes of intracellular solution and 1M $CaCl_2$ at the same position where the boutons were imaged.

ΔG/R measurements from spines and boutons were divided by G_{MAX}/R, yielding the reported values of G/G_{MAX}.

Optical quantal analysis was performed as follows: responses were evoked in spines on basal dendrites with extracellular stimulation, while 6 – 12 spines were scanned simultaneously (for multiple ROI scanning see ref. 52). Responses were sorted into groups of failures and successes by their peak amplitudes. The threshold was set as 2 × standard deviation (SD) of the unfiltered baseline. In most cases this $2 \times SD_{baseline}$ resulted in a clear separation of events as shown in Fig. 3. However in a few cases the distribution of the peak amplitudes was insufficient to unequivocally distinguish between successes and failures. This was the consequence of $[Ca^{2+}]$ transients with small amplitudes (but larger than $2 \times SD_{baseline}$) and slow rise time (Supplementary Fig. 1). These transients could be separated from successes on the basis of their slow rise and delayed onset using the amplitude of the first time derivative of the fluorescent trace and the slope of a linear fit to the rise of the transients (Supplementary Fig. 1f, g). Such slow rising events were not included into the successes.

To allow the comparison of $[Ca^{2+}]$ transients measured in different experiments, we first determined the time of dye equilibration in axon terminals (second and third order branches) within 300 μm from the soma at 40–80 μm in the tissue. Within the first two hours of whole-cell recordings we detected a consistent decrease in the amplitude (64 ± 17% of control) and an increase in the decay time constant (132 ± 13% of control; supplementary Fig. 2) of the $[Ca^{2+}]$ transients, alterations consistent with an increase in dye concentration (300 μM Fluo5F in the pipette)[53]. First we imaged the boutons in line-scan mode (duration of 1 scan: 500 ms) with a laser intensity of 5–6 mW at the back aperture of the objective lens every 2 minutes and repeated the measurements at least 10 times. Analysis of the transients revealed that their amplitudes were stable during the first 6 repetitions (Supplementary Fig. 3). We then performed $[Ca^{2+}]$ measurements on a new set of boutons with only 4–6 repetitions per bouton. These measurements resulted in stable amplitudes and decay times throughout the imaging sessions (Supplementary Fig. 3e and f) and revealed a large variability between boutons in the peak $[Ca^{2+}]$ transients (mean ± SD = 0.13 ± 0.06 G/G_{MAX}; n = 16). Following imaging, the slices were fixed and the biocytin was processed for light- and electron microscopic examinations. To our surprise, despite the fact that there was no sign of photodamage of the imaged boutons, electron microscopic images from 56% of the boutons showed large empty intracellular spaces (Supplementary Fig. 3g), ultrastructural abnormalities never observed following normal perfusion fixation or when looking at non-imaged, biocytin-filled boutons. We then slightly increased the laser intensity (8–10 mW at the back aperture of the objective) to obtain a better signal-to-noise ratio on single fluorescent traces (5-6 mW: S/N = 2.1 ± 0.8 vs. 8-10 mW: S/N = 5.6 ± 3.0), but repeated the line scans only 2-4 times for averaging (Fig. 5). With this protocol we measured $[Ca^{2+}]$ transients in a large number of boutons (n = 84 in 4 animals) without any apparent change in the amplitude or decay of the transients during the experiments and without any change in the baseline fluorescent intensity from the beginning to the end of the imaging sessions. Following fixation, visualization of biocytin and identification of individual imaged boutons we serially sectioned them and found that only 12 % had ultrastructural signs of damage (Supplementary Fig. 3h). These boutons were discarded from our analysis. The data presented in the MS in figure 5 comes from such measurements from boutons showing no signs of ultrastructural photodamage.

Light and electron microscopic identification of the imaged boutons and spines

After recordings, slices were fixed (4% paraformaldehyde, 0.5% glutaraldehyde, 0.2% picric acid in 0.1 M phosphate buffer (PB; pH = 7.4) at 4°C for at least 24 hours), embedded in agarose and re-sectioned at 60 μm thickness. Biocytin was visualized using an avidin-biotin-

horseradish peroxidase complex (Vector Laboratories) followed by a reaction with 3′3-diaminobenzidine tetrahydrochloride as chromogen and 0.01% H_2O_2 as oxidant for 12 minutes. Sections were then postfixed in 1% OsO_4 for 20 minutes, stained in 1% uranyl acetate for 25 minutes, dehydrated in a graded series of ethanol and embedded in epoxy resin (Durcupan). Cells were reconstructed using the Neurolucida system (MicroBrightField Europe, Magdeburg, Germany) attached to a Zeiss Axioscope2 microscope using 40x or 100x oil-immersion objectives. Imaged axon/dendrite segments were then re-embedded and sectioned at 60 nm. Slices (for optimal ultrastructural preservation) from a 16 day-old male Wistar rat were fixed in 4% paraformaldehyde, 1% glutaraldehyde in 0.1M PB, dehydrated, embedded in Durcupan, sectioned at 60 nm or for the quantification of the number of the docked vesicles per active zone at 20 nm. Digital images from serial electron microscopic sections were taken from randomly selected volumes of the str. oriens at a magnification of 10 000 or 20 000 × with a Jeol1011 electron microscopic. Boutons and spines were 3D reconstructed and their volumes and the area of the PSD were measured using the Reconstruct software (http://synapses.clm.utexas.edu/). The area of an active zone was considered to be equal to that of the corresponding PSD[1]. We defined the end of an *en passant* bouton at the point where it's diameter reached the diameter of the average inter-bouton axon.

SDS-digested freeze-fracture replica-labeling (SDS-FRL)

Adult and P16 Wistar rats, $Cav2.1^{+/-}$ and $Cav2.1^{-/-}$ mice[49] (kindly provided by Dr Noboru Suzuki) were deeply anesthetized and were transcardially perfused with ice-cold fixative containing 2% paraformaldehyde in 0.1 M PB for 15 minutes. 80 μm thick sections from the hippocampal CA3 area were cut, cryoprotected in 30% glycerol, frozen with a high-pressure freezing machine (HPM100, Leica Microsystems, Austria) and fractured in a freeze-fracture machine (EM BAF060, Leica) as described in Lorincz and Nusser[54] and Kulik et al.[55]. The fractured faces were coated on a rotating table by carbon (5 nm) with an electron beam gun positioned at 90°, then shadowed by platinum (2 nm) at 60° unidirectionally, followed by a final carbon coating (20 nm). Tissue debris was digested from the replicas with gentle stirring in a TBS solution containing 2.5% SDS and 20% sucrose (pH = 8.3) at 80°C for 18 hours. The replicas were washed in TBS containing 0.05% bovine serum albumin (BSA) and blocked with 1% or 5% BSA in TBS for one hour followed by incubation in the solution of primary antibodies. The following primary antibodies were used: guinea pig anti-Cav2.1 (1:80-1:100) raised against an epitope (amino acids 360–400; ref. 56) corresponding to a sequence in the intracellular loop between domains I and II, rabbit anti-Cav2.1 (1:500; Synaptic Systems, Gottingen, Germany) recognizing a C-terminal domain epitope (amino acids 1921–2212); rabbit anti-Rim1/2 (1:800 or 1:2000; Synaptic Systems, Goettingen, Germany); mouse anti-SNAP-25 (1:1000; Synaptic Systems); mouse anti-synaptobrevin (1:1000; Millipore, Millerica, MA); rabbit anti-syntaxin-1B (1:1000; Synaptic Systems); and rabbit pan-AMPAR (1:2000; Synaptic Systems). Replicas were then incubated in a solution containing the following secondary antibodies: goat anti-rabbit IgGs (GAR) coupled to 10 or 15 nm gold particles (1:50; British Biocell International, Cardiff, UK), goat anti-mouse IgGs coupled to 10 or 15 nm gold particles for (1:50; British Biocell) and goat anti-guinea pig IgGs coupled to 10 nm gold particles for (1:50; British Biocell). Replicas were rinsed in TBS and distilled water, before they were picked up on copper parallel bar grids and examined with a Jeol1011 electron microscope. All antibodies used in this study, except for the pan-AMPAR antibody, recognized intracellular epitopes on their target proteins and consequently were visualized by gold particles on the protoplasmic membrane half (P-face). Background labeling was determined on extracellular membrane halves (E-faces), where no specific signal was expected. The pan-AMPAR antibody recognized an extracellular epitope, therefore gold particles labeling the AMPARs were detected on the E-face. For quantitative analysis, electron micrographs of presynaptic axon terminals were taken

containing active zones broken in their completeness, recognized by loose clusters of IMPs. We used either the rabbit anti-Cav2.1 antibody or a mixture of the rabbit and guinea pig anti-Cav2.1 antibodies to determine the density of gold particles labeling the Cav2.1 subunit in active zones. Gold particle densities obtained with the rabbit or with the mixture of the rabbit and guinea pig antibodies were not significantly different (t-test, $p > 0.05$), therefore they were pooled. For generating random 'gold' distribution patterns in active zones, we digitized the active zones and covered with a fine mesh (8–10 nm). The position of a simulated gold particle within the active zones were generated using the random number generator of MS Excel and was repeated for the same number of times as the number of real gold particles in any given synapse. All inter-'gold' distances were measured in MS Excel and the distribution was compared to that of the experimental data using the Statistica software (StatSoft Inc., Tulsa, OK).

Data analysis and statistical tests

Analysis of electrophysiological and two-photon imaging data was performed using a specialized software (MES, Femtonics). Data were plotted using OriginPro. Correlations between morphological and two-photon imaging data were assessed using linear regression fit to the data (R indicates Pearson's correlation coefficient) when the data was not significantly different from a normal distribution (Kolmogorov-Smirnov test). For the linear regressions in figures 2 and 4, where the data set was too small for testing normality, Spearman correlation was calculated and the correlation coefficients are shown. Statistical significance on the effects of the calcium channel blockers on the peak $[Ca^{2+}]$ transient was assessed with Student's t-test following Kolmogorov-Smirnov normality test. Immunogold densities for Cav2.1 and Rim1/2 were compared in synaptic, extrasynaptic compartments and on E-face membranes (background) using the nonparametric Kruskal-Wallis test. Kolmogorov-Smirnov test was used for comparing the original within synapse inter-gold distance distributions with random distributions. Results were considered significant with $P < 0.05$. Data are presented as mean ± sd. throughout the manuscript.

Supplementary Material

Refer to Web version on PubMed Central for supplementary material.

Acknowledgments

NH and AL are the recipients of Janos Bolyai Scholarships of the Hungarian Academy of Sciences. ZN is supported by Wellcome Trust Equipment and Project Grants (090197/Z/09/Z), a European Research Council Advanced Grant, and a Hungarian National Office for Research and Technology-French National Research Agency TéT Fund (NKTH-Neurogen). AK is supported by a Deutsche Forschungsgemeinschaft (DFG SFB 780) grant. We would like to thank Dr Noboru Suzuki for kindly providing the Cav2.1$^{-/-}$ mice and Dr Andreas Unger for helping with the Cav2.1$^{-/-}$ replica labeling. We would like to thank Eva Dobai and Dora Ronaszéki for their excellent technical assistance, Dr Máté Sümegi for his help with the modeling, Synaptic Systems GmbH for providing the rabbit anti-Cav2.1 antibody, Prof. Erwin Neher and Dr Mark Eyre for their comments on the manuscript, and Dr Helmuth Koester for helpful discussions.

References

1. Schikorski T, Stevens CF. Quantitative ultrastructural analysis of hippocampal excitatory synapses. J. Neurosci. 1997; 17:5858–5867. [PubMed: 9221783]
2. Shepherd GM, Harris KM. Three-dimensional structure and composition of CA3-CA1 axons in rat hippocampal slices: implications for presynaptic connectivity and compartmentalization. J. Neurosci. 1998; 18:8300–8310. [PubMed: 9763474]
3. Atwood HL, Karunanithi S. Diversification of synaptic strength: presynaptic elements. Nat. Rev. Neurosci. 2002; 3:497–516. [PubMed: 12094207]

4. Takumi Y, Ramirez-Leon V, Laake P, Rinvik E, Ottersen OP. Different modes of expression of AMPA and NMDA receptors in hippocampal synapses. Nat. Neurosci. 1999; 2:618–624. [PubMed: 10409387]
5. Racca C, Stephenson FA, Streit P, Roberts JD, Somogyi P. NMDA receptor content of synapses in stratum radiatum of the hippocampal CA1 area. J. Neurosci. 2000; 20:2512–2522. [PubMed: 10729331]
6. Nusser Z, et al. Cell type and pathway dependence of synaptic AMPA receptor number and variability in the hippocampus. Neuron. 1998; 21:545–559. [PubMed: 9768841]
7. Nimchinsky EA, Yasuda R, Oertner TG, Svoboda K. The number of glutamate receptors opened by synaptic stimulation in single hippocampal spines. J. Neurosci. 2004; 24:2054–2064. [PubMed: 14985448]
8. Matsuzaki M, et al. Dendritic spine geometry is critical for AMPA receptor expression in hippocampal CA1 pyramidal neurons. Nat. Neurosci. 2001; 4:1086–1092. [PubMed: 11687814]
9. Harris KM, Stevens JK. Dendritic spines of CA1 pyramidal cells in the rat hippocampus: serial electron microscopy with reference to their biophysical characteristics. J. Neurosci. 1989; 9:2982–2997. [PubMed: 2769375]
10. Fields RD, Ellisman MH. Synaptic morphology and differences in sensitivity. Science. 1985; 228:197–199. [PubMed: 3975637]
11. Atwood HL, Marin L. Ultrastructure of synapses with different transmitter-releasing characteristics on motor axon terminals of a crab, Hyas areneas. Cell Tissue Res. 1983; 231:103–115. [PubMed: 6133625]
12. Propst JW, Ko CP. Correlations between active zone ultrastructure and synaptic function studied with freeze-fracture of physiologically identified neuromuscular junctions. J. Neurosci. 1987; 7:3654–3664. [PubMed: 3500282]
13. Korn H, Mallet A, Triller A, Faber DS. Transmission at a central inhibitory synapse. II. quantal description of release, with a physical correlate for binomial n. J. Neurophysiol. 1982; 48:679–707. [PubMed: 6127375]
14. Murthy VN, Schikorski T, Stevens CF, Zhu Y. Inactivity produces increases in neurotransmitter release and synapse size. Neuron. 2001; 32:673–682. [PubMed: 11719207]
15. Branco T, Marra V, Staras K. Examining size-strength relationships at hippocampal synapses using an ultrastructural measurement of synaptic release probability. J. Struct. Biol. 2010; 172:203–210. [PubMed: 19895891]
16. Reyes A, et al. Target-cell-specific facilitation and depression in neocortical circuits. Nat. Neurosci. 1998; 1:279–285. [PubMed: 10195160]
17. Thomson AM. Activity-dependent properties of synaptic transmission at two classes of connections made by rat neocortical pyramidal axons in vitro. J. Physiol. (Lond.). 1997; 502:131–147. [PubMed: 9234202]
18. Koester HJ, Johnston D. Target cell-dependent normalization of transmitter release at neocortical synapses. Science. 2005; 308:863–866. [PubMed: 15774725]
19. Rozov A, Burnashev N, Sakmann B, Neher E. Transmitter release modulation by intracellular Ca2+ buffers in facilitating and depressing nerve terminals of pyramidal cells in layer 2/3 of the rat neocortex indicates a target cell-specific difference in presynaptic calcium dynamics. J. Physiol. (Lond.). 2001; 531:807–826. [PubMed: 11251060]
20. Losonczy A, Zhang L, Shigemoto R, Somogyi P, Nusser Z. Cell type dependence and variability in the short-term plasticity of EPSCs in identified mouse hippocampal interneurones. J. Physiol. (Lond.). 2002; 542:193–210. [PubMed: 12096061]
21. Xu-Friedman MA, Harris KM, Regehr WG. Three-dimensional comparison of ultrastructural characteristics at depressing and facilitating synapses onto cerebellar Purkinje cells. J. Neurosci. 2001; 21:6666–6672. [PubMed: 11517256]
22. Oertner TG, Sabatini BL, Nimchinsky EA, Svoboda K. Facilitation at single synapses probed with optical quantal analysis. Nat. Neurosci. 2002; 5:657–964. [PubMed: 12055631]
23. Schneggenburger R, Neher E. Intracellular calcium dependence of transmitter release rates at a fast central synapse. Nature. 2000; 406:889–893. [PubMed: 10972290]

24. Bollmann JH, Sakmann B, Borst JG. Calcium sensitivity of glutamate release in a calyx-type terminal. Science. 2000; 289:953–957. [PubMed: 10937999]
25. Bucurenciu I, Bischofberger J, Jonas P. A small number of open Ca^{2+} channels trigger transmitter release at a central GABAergic synapse. Nat. Neurosci. 2009; 13:19–21. [PubMed: 20010820]
26. Neher E. Vesicle pools and Ca^{2+} microdomains: new tools for understanding their roles in neurotransmitter release. Neuron. 1998; 20:389–399. [PubMed: 9539117]
27. Katz B, Miledi R. The role of calcium in neuromuscular facilitation. J. Physiol. (Lond.). 1968; 195:481–492. [PubMed: 4296699]
28. Llinas R, Steinberg IZ, Walton K. Relationship between presynaptic calcium current and postsynaptic potential in squid giant synapse. Biophys. J. 1981; 33:323–351. [PubMed: 6261850]
29. del Castillo J, Katz B. Quantal components of the end-plate potential. J. Physiol. (Lond.). 1954; 124:560–573. [PubMed: 13175199]
30. Koester HJ, Sakmann B. Calcium dynamics associated with action potentials in single nerve terminals of pyramidal cells in layer 2/3 of the young rat neocortex. J. Physiol. (Lond.). 2000; 529:625–646. [PubMed: 11118494]
31. Wu LG, Saggau P. Pharmacological identification of two types of presynaptic voltage-dependent calcium channels at CA3-CA1 synapses of the hippocampus. J. Neurosci. 1994; 14:5613–5622. [PubMed: 8083757]
32. Wheeler DB, Randall A, Tsien RW. Roles of N-type and Q-type Ca^{2+} channels in supporting hippocampal synaptic transmission. Science. 1994; 264:107–111. [PubMed: 7832825]
33. Reid CA, Clements JA, Bekkers JM. Nonuniform distribution of Ca^{2+} channel subtypes on presynaptic terminals of excitatory synapses in hippocampal cultures. J. Neurosci. 1997; 17:2738–2745. [PubMed: 9092595]
34. Masugi-Tokita M, Shigemoto R. High-resolution quantitative visualization of glutamate and GABA receptors at central synapses. Curr. Opin. Neurobiol. 2007; 17:387–393. [PubMed: 17499496]
35. Hagiwara A, Fukazawa Y, Deguchi-Tawarada M, Ohtsuka T, Shigemoto R. Differential distribution of release-related proteins in the hippocampal CA3 area as revealed by freeze-fracture replica labeling. J. Comp. Neurol. 2005; 489:195–216. [PubMed: 15983999]
36. Lisman J. Long-term potentiation: outstanding questions and attempted synthesis. Philos. Trans. R. Soc. Lond. B. Biol. Sci. 2003; 358:829–842. [PubMed: 12740130]
37. Hefft S, Jonas P. Asynchronous GABA release generates long-lasting inhibition at a hippocampal interneuron-principal neuron synapse. Nat. Neurosci. 2005; 8:1319–1328. [PubMed: 16158066]
38. Eggermann E, Bucurenciu I, Goswami SP, Jonas P. Nanodomain coupling between Ca^{2+} channels and sensors of exocytosis at fast mammalian synapses. Nat. Rev. Neurosci. 2012; 13:7–21. [PubMed: 22183436]
39. Bucurenciu I, Kulik A, Schwaller B, Frotscher M, Jonas P. Nanodomain coupling between Ca^{2+} channels and Ca^{2+} sensors promotes fast and efficient transmitter release at a cortical GABAergic synapse. Neuron. 2008; 57:536–545. [PubMed: 18304483]
40. Mennerick S, Matthews G. Ultrafast exocytosis elicited by calcium current in synaptic terminals of retinal bipolar neurons. Neuron. 1996; 17:1241–1249. [PubMed: 8982170]
41. Christie JM, Chiu DN, Jahr CE. Ca^{2+}-dependent enhancement of release by subthreshold somatic depolarization. Nat. Neurosci. 2011; 14:62–68. [PubMed: 21170054]
42. Fedchyshyn MJ, Wang LY. Developmental transformation of the release modality at the calyx of Held synapse. J. Neurosci. 2005; 25:4131–4140. [PubMed: 15843616]
43. Meinrenken CJ, Borst JG, Sakmann B. Calcium secretion coupling at calyx of held governed by nonuniform channel-vesicle topography. J. Neurosci. 2002; 22:1648–1667. [PubMed: 11880495]
44. Ohana O, Sakmann B. Transmitter release modulation in nerve terminals of rat neocortical pyramidal cells by intracellular calcium buffers. J. Physiol. (Lond.). 1998; 513:135–148. [PubMed: 9782165]
45. Llinas R, Sugimori M, Silver RB. Microdomains of high calcium concentration in a presynaptic terminal. Science. 1992; 256:677–679. [PubMed: 1350109]

46. DiGregorio DA, Peskoff A, Vergara JL. Measurement of action potential-induced presynaptic calcium domains at a cultured neuromuscular junction. J. Neurosci. 1999; 19:7846–7859. [PubMed: 10479687]
47. Frank T, Khimich D, Neef A, Moser T. Mechanisms contributing to synaptic Ca^{2+} signals and their heterogeneity in hair cells. Proc. Natl. Acad. Sci. USA. 2009; 106:4483–4488. [PubMed: 19246382]
48. Liu KS, et al. RIM-binding protein, a central part of the active zone, is essential for neurotransmitter release. Science. 2011; 334:1565–1569. [PubMed: 22174254]
49. Kulik A, et al. Immunocytochemical localization of the a_{1A} subunit of the P/Q-type calcium channel in the rat cerebellum. Eur. J. Neurosci. 2004; 19:2169–2178. [PubMed: 15090043]
50. Tanaka J, et al. Number and density of AMPA receptors in single synapses in immature cerebellum. J. Neurosci. 2005; 25:799–807. [PubMed: 15673659]
51. Gulyas AI, et al. Parvalbumin-containing fast-spiking basket cells generate the field potential oscillations induced by cholinergic receptor activation in the hippocampus. J. Neurosci. 2010; 30:15134–15145. [PubMed: 21068319]
52. Lorincz A, Rozsa B, Katona G, Vizi ES, Tamas G. Differential distribution of NCX1 contributes to spine-dendrite compartmentalization in CA1 pyramidal cells. Proc. Natl. Acad. Sci. USA. 2007; 104:1033–1038. [PubMed: 17215351]
53. Maravall M, Mainen ZF, Sabatini BL, Svoboda K. Estimating intracellular calcium concentrations and buffering without wavelength ratioing. Biophys. J. 2000; 78:2655–2667. [PubMed: 10777761]
54. Lorincz A, Nusser Z. Molecular identity of dendritic voltage-gated sodium channels. Science. 2010; 238:906–909. [PubMed: 20466935]
55. Kulik A, et al. Compartment-dependent colocalization of Kir3.2-containing K^+ channels and GABAB receptors in hippocampal pyramidal cells. J. Neurosci. 2006; 26:4289–4297. [PubMed: 16624949]
56. Miyazaki T, et al. Cav2.1 in cerebellar Purkinje cells regulates competitive excitatory synaptic wiring, cell survival, and cerebellar biochemical compartmentalization. J. Neurosci. 2012; 32:1311–1328. [PubMed: 22279216]

Europe PMC Funders Author Manuscripts

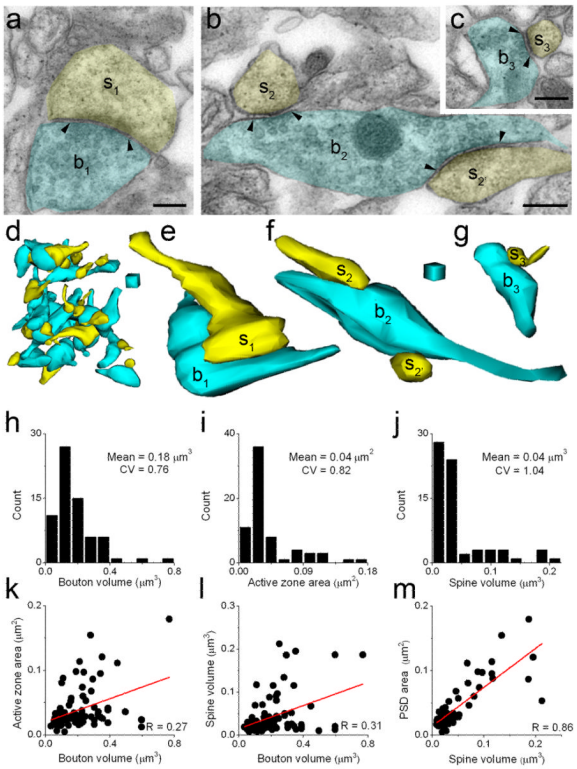

Figure 1.

Morphological diversity of glutamatergic axon terminals in the CA3 region of the rat hippocampus. (**a-c**) Electron micrographs show synaptic contacts of axon collaterals (b, blue) of CA3 pyramidal cells and their postsynaptic spines (s, yellow). Terminals differ in their size, active zone (demarcated by arrowheads, same length as the corresponding PSD) area and the number and the size of the postsynaptic spines. (**d**) 3D reconstruction of a randomly chosen volume in the stratum oriens. Axon terminals are shown in blue and postsynaptic spines in yellow. (**e-g**) Higher magnification of three terminals shown in panel **d**, demonstrating large variability in their size and their postsynaptic spines. (**h-j**) Distributions of measured parameters in the total reconstructed population of terminals in n = 1 animal. (**k-l**) Bouton volume shows a weak, but significant correlation with the active zone area ($p = 0.0023$, n = 68 boutons), while no significant correlation was found with the volume of the individual postsynaptic spines (**l,** $p = 0.081$, n = 83 spines). (**m**) Spine volume and corresponding PSD area are tightly correlated ($p < 0.0001$, n = 83 spines and PSDs). Scale bars represent 0.2 μm (**a-c**) and sides of the cubes are 0.2 μm (**d**) and 0.1 μm (**e-g**).

Europe PMC Funders Author Manuscripts

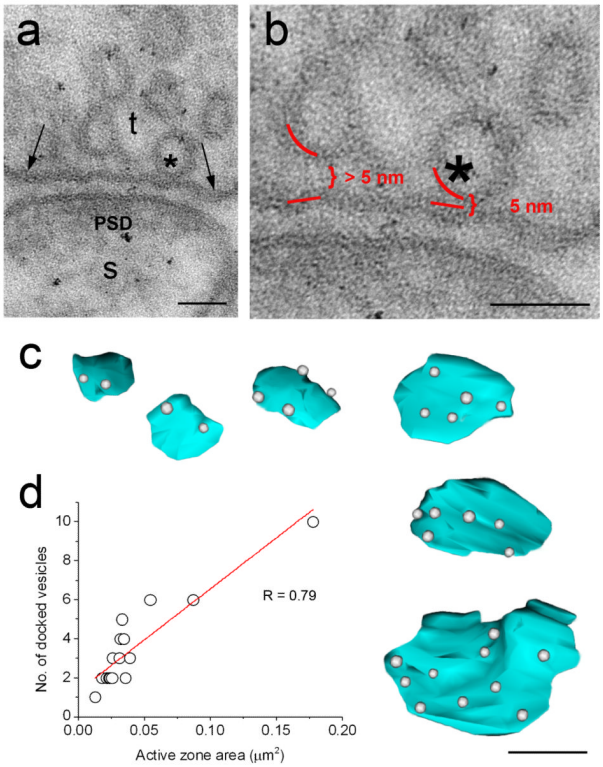

Figure 2.

The number of the docked vesicles correlates linearly with the size of the active zone. (**a**) An electron microscopic image of a synaptic contact between a CA3 pyramidal cell spine (s) and axon terminal (t) in the str. oriens taken from a 20 nm thick electron microscopic section. The postsynaptic density (PSD) is clearly visible and arrows demarcate the active zone. One of the vesicles (*) is closely apposed to the presynaptic membrane. (**b**) Higher magnification view of the active zone region showing that a gap between the presynaptic- and vesicle membranes can not be resolved, the distance between the middle of the 2 membranes is <5 nm. Vesicles with such a small distance from the active zone plasma membrane are considered to be docked. (**c**) 3D reconstructions of active zones (light blue) from serial 20 nm thick electron microscopic sections (number of sections used for reconstruction ranged 11 – 22). White spheres correspond to docked vesicles. If a vesicle appeared on consecutive sections in the same position, was considered to be cut in half and was counted as a single vesicle. (**d**) Active zone area shows a tight, positive correlation with the number of the docked vesicles (n = 15 active zones in n = 1 animal). Scale bars represent: 50 nm (**a**-**b**), 200 nm (**c**)

Europe PMC Funders Author Manuscripts

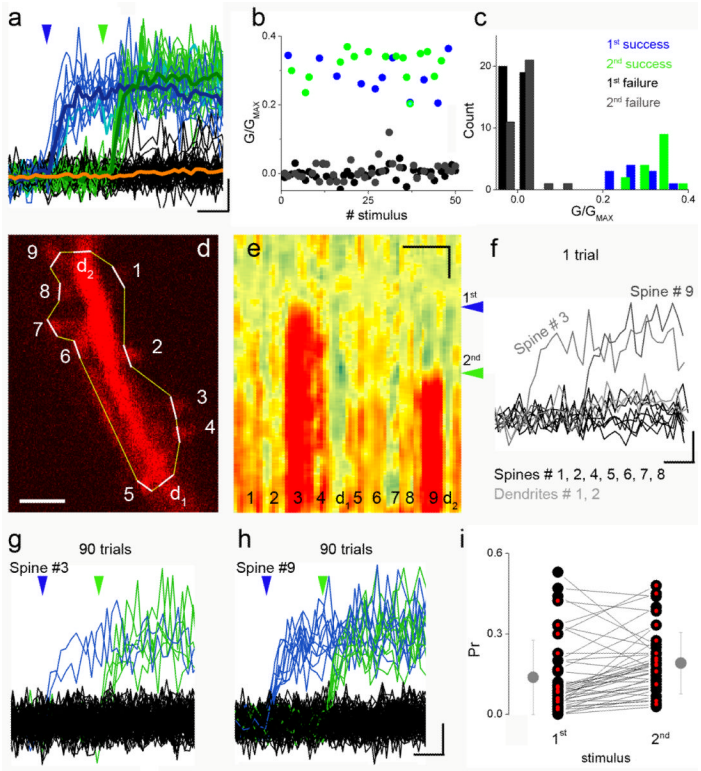

Figure 3.

Determining the release probability of axon terminals with optical quantal analysis. (**a**) Changes in fluorescent intensity measured with line scans in a representative spine head of a CA3 pyramidal cell basal dendrite as a consequence of Ca^{2+} influx through NMDA receptors. A pair of synaptic responses were evoked by extracellular stimulation (100 ms inter-stimulus interval, the time of the stimuli are indicated by the arrowheads) of local axon collaterals in the str. oriens. Successes for the first and second stimuli are colored in blue and green, respectively. A double event is shown in light blue, whereas failures are shown in black (throughout the figure). Thick traces represent averages. The amplitude values were determined by averaging within a 40 ms window starting 50 ms after the stimuli. (**b**) Amplitudes of fluorescent responses plotted against time. The peak amplitudes of successes and the fluorescence intensities of failures measured over the same time window were stable (same data as in **a**). (**c**) Histograms of response amplitudes demonstrate that failures can be clearly distinguished from successes (same data as in **a-b**). (**d**) A two-photon image of a basal dendritic segment with multiple spines. The line indicates the path of the focal spot in line scanning mode. White lines correspond to the segments from where data were collected with a reduced, constant scanning speed. Numbers correspond to individual spines throughout panels **d-h**. (**e**) Pseudo-colored representation of the line scans across spine heads and the dendritic shaft vs. scanning time (450 ms). Arrowheads indicate the stimulations. Fluorescence increased rapidly in spine #3 and #9 after the first and the second stimulations, respectively. (**f**) The same data as in panel **e** is plotted here in a different way. Fluorescent traces in two dendritic shafts (light grey) and in nine spines (7 did not (black) and two (grey) displayed rapid [Ca^{2+}] transients) are shown. (**g-h**) 90 superimposed response traces to paired stimulations in spines #3 and #9 demonstrate differences in release probability (P_R^{1st}: 0.021 for #3 and 0.1 for #9). (**i**) Summary graph showing the P_R^{1st} and P_R^{2nd} of individual spines (black dots; n = 43, n = 14 animals). Means and standard deviations are shown in grey. Note that few synapses had zero P_R^{1st}. Red symbols represent

Europe PMC Funders Author Manuscripts

electron microscopically analyzed synapses (n = 14). On average, the synapses showed an increase in release probability (paired pulse facilitation). Scale bars represent 50 ms and 0.1 G/G_{MAX} (**a, f, g, h**), 2 μm (**d**), 2 μm and 50 ms (**e**).

Europe PMC Funders Author Manuscripts

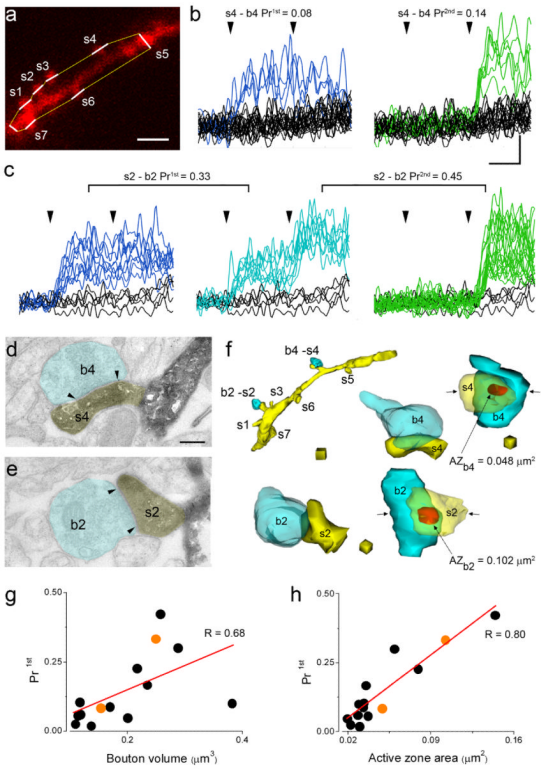

Figure 4.

Post hoc ultrastructural analysis of synapses following two-photon imaging. (**a**) A two-photon image of a CA3 pyramidal cell basal dendritic segment with multiple spines. Two out of seven spines (s2 and s4) displayed [Ca^{2+}] transients in response to extracellular stimulations. (**b**) Multiple responses to paired extracellular stimulations in s4. Successes for the 1st and 2nd stimuli are separated for clarity. (**c**) Same as in panel **b** for spine #2. At higher release probability, there is an increased chance that release occurs for both stimuli (light blue traces) (**d-e**) Electron micrographs showing presynaptic axon terminals (b2 and b4, pseudo-colored in blue) that established synapses onto the imaged spines (s2, s4, active zones are marked with arrowheads). (**f**) 3D reconstruction of the whole dendritic segment (yellow) and two axon terminals (b2 and b4 blue, upper left). Enlarged 3D view of the terminals (b2, b4) and the corresponding spines (s2, s4) from 2 different perspectives; on the left the boutons are semitransparent, same direction as the electron microscopic images, on the right the spines are semitransparent and the reconstructions are rotated to achieve an *en face* view of the active zones (orange). Note the differences in the size of the active zones and the P_R^{1st}. Apposing arrows indicate the positions of the electron microscopic sections from which images are shown in panels **d-e**. (**g, h**) Bouton volume shows a weak (**g**, $p = 0.038$, $n = 14$ synapses from 6 animals) whereas the active zone area displays a tight and significant ($p < 0.0001$) positive correlation (**h**) with the P_R^{1st}. Orange dots indicate b2 and b4. Scale bars represent 2 µm **(a),** 50 ms and 0.1 G/G_{MAX} (**b, c**), 0.2 µm (**d-e),** sides of the scale cubes 0.5 µm (**f** upper left) 0.1 µm (rest of **f**).

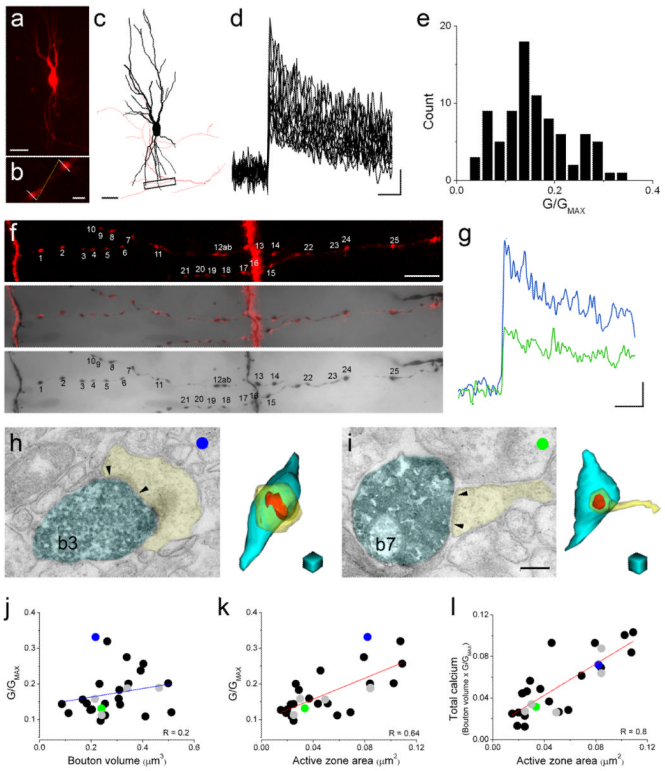

Figure 5.

Measurement of volume averaged [Ca^{2+}] transients in CA3 pyramidal cell local axon terminals. (**a**) Two-photon image of a CA3 pyramidal cell filled with Alexa594 (red) and Fluo5F. (**b**) Higher magnification view of two boutons. White lines indicate the position of the line scans. (**c**) Neurolucida reconstruction of the cell shown in panel **a**. The majority of the axon (red) is truncated for clarity. Boxed area, enlarged in panel **f,** showing the scanned axon collateral segment. (**d**) Individual [Ca^{2+}] transients in 25 axon terminals (shown in panel **f**) of the pyramidal cell. (**e**) Distribution of the peak amplitudes measured in 4 cells. (**f**) The two-photon image (upper panel) is superimposed (middle panel) on the transmitted light microscopic image (lower panel) following aldehyde fixation and visualization of the intracellular biocytin with diaminobenzidine. (**g**) [Ca^{2+}] transients from two boutons are shown (b3, b7). (**h-i**) Electron microscopic images (left) and 3D reconstructions (right) of two boutons (b3: blue, b7: green) that established excitatory synapses on pyramidal cell spines (yellow, arrowheads demarcate the PSDs). (**j**) Peak amplitude of the [Ca^{2+}] transients does not correlate with the bouton volume ($p = 0.3$, n = 27 boutons, n = 4 cells, n = 4 animals). (**k**) The peak [Ca^{2+}] shows a significant ($p < 0.001$) positive linear correlation with the active zone area. (**l**) Total fluxed calcium, calculated from the peak [Ca^{2+}] transients and the volume of the boutons, correlates tightly ($p < 0.001$) with the active zone area. Blue and green circles represent the two boutons shown in panels **h** and **i**, respectively. Grey circles represent the remaining boutons from the string shown in **f**. Scale bars represent: 50 μm (**a, c**), 2 μm (**b**), 50 ms, 0.05 G/G_{MAX} (**d, g**), 10 μm (**f**), 0.2 μm (**h, i**), sides of the cubes: 0.2 μm (**h, i**)

Europe PMC Funders Author Manuscripts

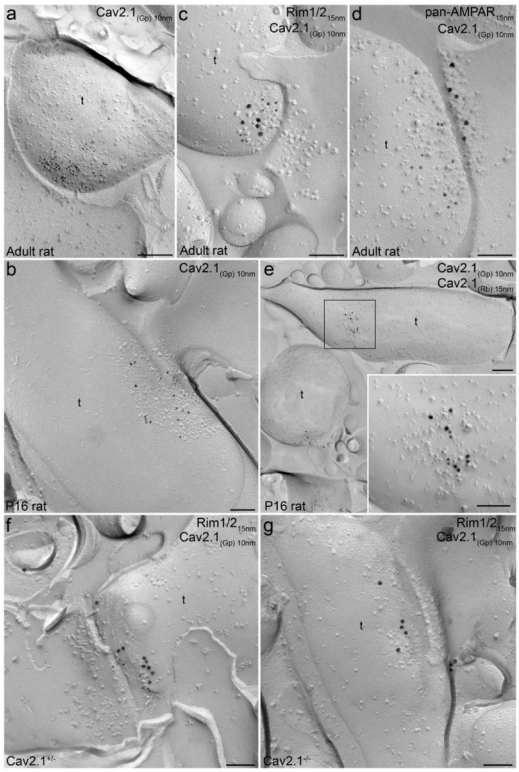

Figure 6.

The Cav2.1 subunit is confined to the active zone of presynaptic axon terminals in the stratum oriens of the hippocampal CA3 area. (**a, b**) SDS-digested freeze-fracture replica-labeling of the Cav2.1 subunit on the P-face of axon terminals (t) in an adult (**a**) and a P16 rat (**b**). Gold particles are enriched in putative active zones of the terminals indicated by the loose cluster of intramembrane particles. (**c**) The active zone of a presynaptic axon terminal is co-labeled for the Cav2.1 subunit (10 nm gold) and Rim1/2 (15 nm gold) in an adult rat. (**d**) Gold particles labeling the Cav2.1 subunit (10 nm gold) are concentrated on the P-face of a presynaptic active zone of an excitatory synapse facing the E-face of the postsynaptic membrane enriched in AMPA receptors (15 nm gold). (**e**) Two Cav2.1 antibodies, one raised in a rabbit (Rb) and another one in a guinea pig (Gp) against different epitopes, label the same presynaptic active zone. **(e inset)** A high magnification image of the active zone shown in the boxed area in **e**. (**f, g**) active zones identified by Rim1/2 immunolabeling (15 nm gold) are co-labeled for the Cav2.1 subunit (10 nm gold) in a $Cav2.1^{+/-}$ mouse (**f**), but small gold particles labeling the Cav2.1 subunit could not be found in $Cav2.1^{-/-}$ mice (**g**). Scale bars: 200 nm **(a, e**), 100 nm (**b-d, e inset, f, g**).

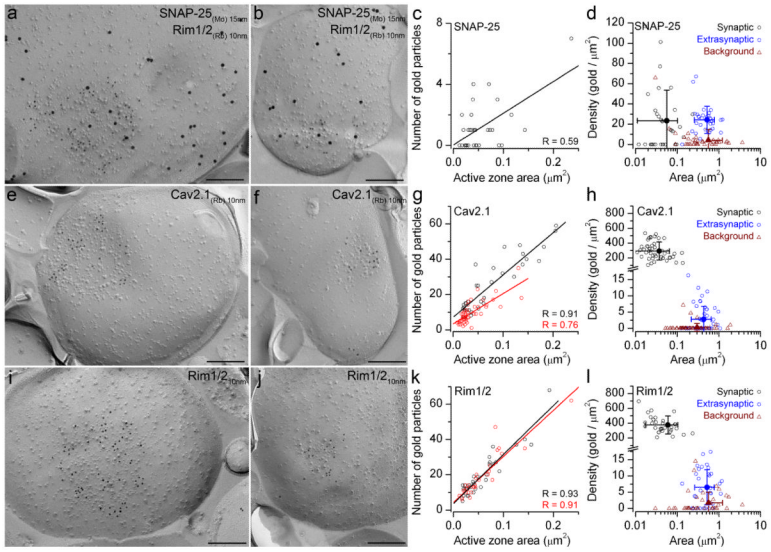

Figure 7.

The number of Cav2.1 subunits and Rim1/2 proteins correlates with the active zone area. (**a, b**) SDS-FRL labeling of SNAP-25 in a large (**a**) and a small (**b**) active zone. (**c**) Correlation of the number of gold particles labeling SNAP-25 with the active zone area (n = 32 in rat#2). (**d**) Density of gold particles within presynaptic active zones (mean ± SD = 23.5 ± 30.3, n = 32) and in the surrounding extrasynaptic axonal plasma membranes (mean ± SD = 24.3 ± 13.4, n = 32), in comparison with the background labeling calculated on E-face plasma membranes (mean ± SD = 4.1 ± 10.6, n = 40; $p_{synaptic} < 0.01$, $p_{extrasynaptic} < 0.01$). (**e**, **f**) SDS-FRL labeling of the Cav2.1 subunit in a large (**e**) and a small (**f**) active zone. (**g**) Correlation of the number of gold particles labeling the Cav2.1 subunit with the active zone area in two rats (rat#1: black open circles, n = 34 active zones; rat#2: red open circles, n = 49 active zones). (**h**) Density of gold particles labeling the Cav2.1 subunit within presynaptic active zones (mean ± SD = 395.8 ± 154.8, n = 34 in rat#1) and in the surrounding extrasynaptic axonal plasma membrane (mean ± SD = 1.6 ± 2.4, n = 32 in rat#1) in comparison with the background labeling calculated on E-face plasma membranes (mean ± SD = 0.6 ± 2.3, n = 39; psynaptic < 0.01, pextrasynaptic = 0.73). (**i, j**) SDS-FRL labeling of Rim1/2 in a large (**i**) and a small (**j**) active zone. (**k**) Correlation of the number gold particles labeling Rim1/2 with the active zone area (rat#1: black open circles, n = 32 active zones; rat#2: red open circles, n = 32 active zones). (**l**) Density of gold particles labeling the Rim1/2 within the presynaptic active zone (mean ± SD = 374.2 ± 110, n = 32 in rat#2) and in the surrounding extrasynaptic axonal plasma membrane (mean ± SD = 6.5 ± 5.4, n = 32 in rat#2), in comparison with the background labeling calculated on E-face plasma membranes (mean ± SD = 1.7 ± 3.3, n = 40; $p_{synaptic} < 0.01$, $p_{extrasynaptic} = 0.025$). Scale bars: 200 nm.

Europe PMC Funders Author Manuscripts

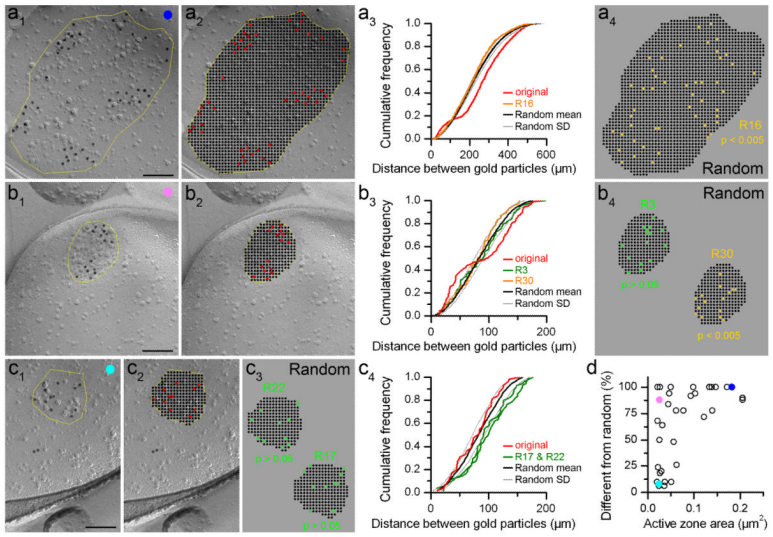

Figure 8.

Non-random distribution of the Cav2.1 subunits within the active zones. (**a-c**) Examples of different gold particle distributions within a large (**a**) and two small (**b** and **c**) active zones. (**a_1**) SDS-FRL replica image showing the distribution of gold particles in a large active zone (0.182 μm^2). (**a_2**) The same active zone area is covered with a mesh (10 nm). The positions of the 47 gold particles are shown in red. (**a_3**) Cumulative probability distributions of the inter-gold distances of the experimental data (red) and the mean (black) ± SD (grey) of 50 random distributions. R16 (orange) is an individual random distribution (shown in **a_4**). The original gold particle distribution was significantly different ($p < 0.01$) from all of the 50 random distributions. (**a_4**) Visualization of a random distribution within the active zone. (**b_1-b_4**) Same as **a_1-a_4**, but for a small synapse (0.025 μm^2) that contained only 15 gold particles. (**b_4**) Visualization of two random distributions, one that gave an inter-'gold' distance distribution that was significantly different (yellow) and another one that was not different (green) from the data. (**c_1-c_4**) Same as **a_1-a_4**, but showing a small active zone (0.024 μm^2, containing 11 gold particles) in which the inter-gold distance distribution was rarely different (4 out of 50) from random distributions. (**d)** Percentage of the simulations in which the experimentally determined inter-gold distance distributions were different from random inter-gold distance distributions in individual active zones, plotted as a function of the active zone area (n = 34 active zones, rat #1). The three active zones shown in panels **a-c** are indicated by the three colored symbols. Note that for large synapses, there is a larger proportion of the active zones in which the distribution of Cav2.1 channels significantly differ from random distribution.